MDPI

Article

Film Thickness Effect in Restructuring NiO into LiNiO$_2$ Anode for Highly Stable Lithium-Ion Batteries

Thang Phan Nguyen [ID] and Il Tae Kim *[ID]

Department of Chemical and Biological Engineering, Gachon University, Seongnam-si 13120, Gyeonggi-do, Republic of Korea; npthang@gachon.ac.kr
* Correspondence: itkim@gachon.ac.kr

Abstract: The long-term stability of energy-storage devices for green energy has received significant attention. Lithium-ion batteries (LIBs) based on materials such as metal oxides, Si, Sb, and Sn have shown superior energy density and stability owing to their intrinsic properties and the support of conductive carbon, graphene, or graphene oxides. Abnormal capacities have been recorded for some transition metal oxides, such as NiO, Fe$_2$O$_3$, and MnO/Mn$_3$O$_4$. Recently, the restructuring of NiO into LiNiO$_2$ anode materials has yielded an ultrastable anode for LIBs. Herein, the effect of the thin film thickness on the restructuring of the NiO anode was investigated. Different electrode thicknesses required different numbers of cycles for restructuring, resulting in significant changes in the reconstituted cells. NiO thicknesses greater than 39 μm reduced the capacity to 570 mAh g^{-1}. The results revealed the limitation of the layered thickness owing to the low diffusion efficiency of Li ions in the thick layers, resulting in non-uniformity of the restructured LiNiO$_2$. The NiO anode with a thickness of approximately 20 μm required only 220 cycles to be restructured at 0.5 A g^{-1}, while maintaining a high-rate performance for over 500 cycles at 1.0 A g^{-1}, and a high capacity of 1000 mAh g^{-1}.

Keywords: lithium-ion batteries; restructuring anode; NiO; LiNiO$_2$; ex situ XRD

1. Introduction

The unprecedented interest in green energy is pursued to solve the global problems of conventional fuel depletion and environmental pollution [1,2]. The utilization of various renewable sources, including solar, tidal, and wind energy, has demonstrated the ability to meet energy demands without producing greenhouse gases [3,4]. The expansion of renewable energy sources necessitates high energy densities and stable energy storage systems [5,6]. Furthermore, conventional modes of transportation are gradually being replaced by electric vehicles as part of the efforts to reduce daily emissions [7,8]. Consequently, the development of capacitors and batteries plays a pivotal role in shaping the future of energy storage systems [5,9–11]. Since their invention to the present day, lithium-ion batteries (LIBs) have acquired considerable popularity and can be applied in cell phones, portable devices, vehicles, and industrial machinery [12–14].

Anode materials for LIBs have achieved significant progress in terms of lifespan, energy density, and specific capacity [15–20]. Recently, several superior anode materials have been proposed, including nanomaterials such as three-dimensional (3D) porous Si, Fe$_2$O$_3$, and NiO [21–30]. Jia et al. proposed the use of porous silicon structures with CNTs for the LIB anode, which could deliver a high capacity of ~750 mAh g^{-1} [21]. The combination of porous Si with CNT and carbon or graphene achieved a stable anode with high physical stability. Zhu et al. demonstrated a 3D structure of Si nanoparticles in a graphene/carbon matrix that prevented the volume expansion of Si and further stabilized the structure, delivering a high capacity of approximately 2000 mAh g^{-1} [31]. The 3D Si anode could deliver a capacity of ~600 mAh g^{-1} at a high current rate 28.0 A g^{-1}.

Transition metal oxides (TMOs) also received significant attention owing to their air stability, environmental friendliness, and high theoretical capacity (>500 mAh g^{-1}) [32]. Moreover, the TMO anode with affordable modifications showed a high stability for LIBs [33–35]. Jiang et al. integrated porous Fe_2O_3 into a 3D graphene framework, which exhibited high stability for over 1200 cycles; delivered a reversible capacity of ~1130 mAh g^{-1} [26]. Porous Fe_2O_3 on a graphene aerogel structure showed high flexibility and a significant rate performance at 5 A g^{-1} with a capacity of ~500 mAh g^{-1}. Hassan et al. fabricated complex nanostructured α-Fe_2O_3 using the molten salt method [27]. The nanosized α-Fe_2O_3 as a LIB anode exhibited a high capacity of ~1200 mAh g^{-1} and recovered its fading capacity after 100 cycles. After 600 cycles, this anode material delivered a high capacity of ~1900 mAh g^{-1}, which is much higher than the theoretical capacity of ~1000 mAh g^{-1}. The NiO nanostructure also received great attention for its various electrical/optical applications, including capacitors, gas sensors, solar cells, and magnetic applications [36–40]. NiO has a theoretical capacity of ~720 mAh g^{-1}, which is more than twice that of graphene [41]. Moreover, several reports demonstrated that NiO anodes can deliver a higher capacity than theoretical capacity [32,42,43]. Fan et al. fabricated ultrathin NiO embedded in the 3D mesoporous carbon CMK-3, delivering a high capacity of approximately 1000 mAh g^{-1} at 0.1 A g^{-1} [42]. The NiO/CMK-3 anode could exhibit a high capacity of over 800 mAh g^{-1} at a current rate of 0.8 A g^{-1}. Wang et al. reported that the self-growth of NiO on Ni foam could boost the first discharge capacity over 900 mAh g^{-1} [44]. In addition, 3D Ni foam provides a large surface area and facilitates the electrochemical reaction, thereby enhancing the rate performance up to 4C with a high capacity of ~500 mAh g^{-1}. Thus, the nanoporous structure of active material can facilitate the insertion of lithium ion, resulting in the improvement of the LIB's anode performance. In addition, self-healing anode materials with a combination of healable conductive polymers are also attractive [45–50]. Chen et al. synthesized a self-healing polymer based on ether-thioureas as a binder for silicon anodes [51]. This polymer could effectively enhance the performance of the silicon anode, and achieved a high-capacity retention of ~85% after 250 cycles at a current of 4.2 A g^{-1}. Jin et al. applied a self-healing solid electrolyte interface (SEI) layer to protect the silicon anode, which significantly enhanced the stability of the anode with an average coulombic efficiency of 99.9% [47]. However, the most significant problem lies in the active material. Therefore, even with healable polymers, LIB capacity still faces gradual degradation.

A recent study reported that the restructuring of NiO into $LiNiO_2$/Ni stabilized its structure during lithium insertion and extraction [28]. Upon cycling at a high rate of 500 mA g^{-1}, lithium ions initially degrade the NiO structure for the first 200 cycles, followed by the rebuilding of the NiO structure into $LiNiO_2$/Ni. The layered structure of $LiNiO_2$ enhances the insertion and extraction of lithium ions in the anode material, allowing the devices to endure over 10,000 cycles at 1.0 A g^{-1} while almost fully recovering their capacity at 0.1 A g^{-1}. The high specific capacity of restructured cells was approximately 1200 mAh g^{-1}, which significantly exceeded the theoretical capacity of approximately 720 mAh g^{-1} [32,52]. This enhancement can be attributed to three main phenomena [53]: (1) additional storage resulting from conversion reactions, (2) increased surface area owing to the formation of the solid electrolyte layer, and (3) alterations in morphology, creating additional storage spaces. Although the first and second factors appear to depend on the materials used, the third factor may be influenced by the thickness of the active materials. In a previous study, we restructured NiO to $LiNiO_2$ to achieve an ultra-long cycling performance in LIBs. It exhibited ultra-stable cycling properties for 10,000 cycles at 10.0 A g^{-1} and was highly restored at a current rate of 0.1 A g^{-1} with a capacity of ~1200 mAh g^{-1}. In this study, we investigated the effect of NiO thickness on the performance of the restructuring process, unveiling the anomalous capacity observed in previous studies [28]. The results showed that the electrode thickness affects the restructuring process and capacity of the NiO anode. With the aid of the necessary characterizations including ex situ XRD and ex situ SEM, changes in the morphology, structure, and electrical properties of the restruc-

tured NiO anodes illustrated that the electrode thickness affects the overall electrochemical performance, where optimal conditions are achieved.

2. Materials and Methods

2.1. Materials

Nickel (II) chloride hexahydrate ($NiCl_2 \cdot 6H_2O$, 98%), N-methyl 2-pyrrolidinone (NMP, anhydrous, 99.5%), and polyvinylidene fluoride powder (PVDF, MW 534,000) were purchased from Sigma-Aldrich Inc. (St. Louis, MO, USA). Absolute ethanol, Super P amorphous carbon black (C, ~40 nm, 99.99%), and ammonia solution (NH_3, 28%) were procured from Alpha Aesar Inc. (Haverhill, MA, USA).

2.2. Fabrication of NiO Porous Nanosheets (NSs)

NiO NSs were synthesized according to previously reported methods. Briefly, 3.5 mmol of $NiCl_2 \cdot 6H_2O$ was dissolved in 30 mL of a solution of deionized water (DIW) and ethanol (DIW: ethanol volume ratio = 1:1). The $Ni(OH)_2$ NS precursor was prepared by adding dropwise 10 mL of 5 M NH_4OH to the $NiCl_2$ solution. Then, the reaction mixture was transferred into a 50 mL Teflon line stainless steel autoclave and heated at 200 °C for 8 h in an oven. The $Ni(OH)_2$ precipitate was washed thrice with DI water, then freeze-dried at -80 °C for 3 days using a freeze dryer (Labconco Corp., Kansas, MO, USA). Finally, the porous NiO NSs were obtained by calcination of $Ni(OH)_2$ powder at 600 °C for 2 h in air with a heating rate of 5 °C min^{-1}. The obtained gray powder of NiO NSs was ground for further use.

2.3. Material Characterization

The structures and morphologies of the samples were analyzed using X-ray diffraction (XRD; SmartLab, Rigaku, Tokyo, Japan), transmission electron microscopy (TEM; TECNAI G2F30, FEI Corp., Hillsboro, OR, USA), and field emission scanning electron microscopy (FESEM; Hitachi S4700, Tokyo, Japan) analyses. The morphologies and thicknesses of the NiO thin films were observed using digital microscopy (DM; VHX-7000, Keyence Corp., Osaka, Japan). The surface area and pore size were analyzed using the Brunauer–Emmett–Teller (BET) method with ASAP 2020 (Micromeritics, Norcross, GA, USA).

2.4. Electrochemical Measurements

To evaluate the electrochemical properties of the NiO NS anode material, a half-cell structure was employed using coin-type cells (CR 2032, Rotech Inc., Gwangju, Republic of Korea). The lithium foil was used as the counter electrode. The standard electrolyte was a solution of 1.0 M $LiPF_6$ in diethylene carbonate and ethylene carbonate (1:1, v/v). Polyethylene circular disks were used as the separator. A slurry was prepared by mixing NiO active material, conductive Super P, and a binder of PVDF (weight ratio of 70:15:15) in NMP. The slurry was then casted on Cu foils and dried at 75 °C in a vacuum oven for 1 day to completely stop bubble formation and remove NMP. Then, the electrodes were punched into 12 mm diameter circular disks. To investigate the thickness effect of NiO in the restructuring process, NiO electrodes with various thicknesses (16–50 μm), corresponding to the areal loading mass of 1.0–3.5 mg cm^{-2}, were prepared. The samples were labeled N1, N2, N3, and N4 with increasing mass loadings from 1.0, 1.5, 2.2, and 3.5 mg cm^{-2}, respectively. The electrochemical discharge/charge analysis of the cells was conducted using a battery cycle tester (WBCS3000, WonAtech Co., Ltd., Seocho-gu, Seoul, Republic of Korea). The restructuring NiO was conducted at 0.5 A g^{-1} until a stable capacity was achieved. A ZIVE MP1 apparatus (WonAtech Co., Ltd., Seocho-gu, Seoul, Republic of Korea) was used to measure cyclic voltammetry (CV), the galvanostatic intermittent titration technique (GITT), and electrochemical impedance spectroscopy (EIS) analyses. EIS measurements were performed in a frequency range of 100 kHz to 0.1 Hz. GITT measurements were conducted at 10 mA g^{-1} with a current pulse time of 10 min and a relaxation time of 10 min. All anodes were tested for restructuring processes (cycling

performance) at 0.5 A g^{-1} until the capacity began to decrease or the capacity stabilized over 10 cycles.

3. Results

Ni(OH)$_2$ precursors were prepared by the precipitation method of NiCl$_2$ in a basic NH$_4$OH solution. Hexagonal Ni(OH)$_2$ consists of NiO with a layered structure with intercalation of water molecules. Hydrothermal synthesis assisted in the formation of a uniform structure and high-quality Ni(OH)$_2$ nanosheets (NSs). As shown in Figure 1a,b, very thin and large Ni(OH)$_2$ NSs were obtained in the range of 1–5 μm. The obtained NiO after calcination at 600 °C had a large porosity owing to its rapid transformation from hexagonal Ni(OH)$_2$ to a cubic NiO structure (Figure 1c,d). The SEM image reveals that NiO NSs with a wide range of sizes, from 20 nm to few microns, consist of several holes and free spaces both on the surface and at the interfaces. This played an important role in the reconstruction of LiNiO$_2$ during high-current charging. The grain size of NiO was analyzed using SEM images and the number of small NSs with a size of ~20–40 nm is about 60–70%, as shown in Figure S1. The XRD pattern of NiO with the plot of function of the diffractive angle θ is shown in Figure S2. According to the Willamson–Hall method, the crystalline size (*D*) could be calculated by the following equation [54,55]:

$$\beta Cos\theta = \frac{k\lambda}{D} + 4\varepsilon Sin\theta \tag{1}$$

where λ, θ, β, and k are the Cu Kα wavelength, diffractive angle, full-width at half maximum of the diffractive angle and Scherrer constant; ε is the micro-strain. Therefore, ε is the slope of plot between $\beta Cos\theta$ and $Sin\theta$. $\frac{k\lambda}{D}$ can be obtained from the intercept of that plot. Therefore, D_{NiO} was about 50 nm. The results are in good agreement with that of the SEM image, while the small NiO NSs are highly distributed, and the amount of those with a size of a few μm is less than 5%.
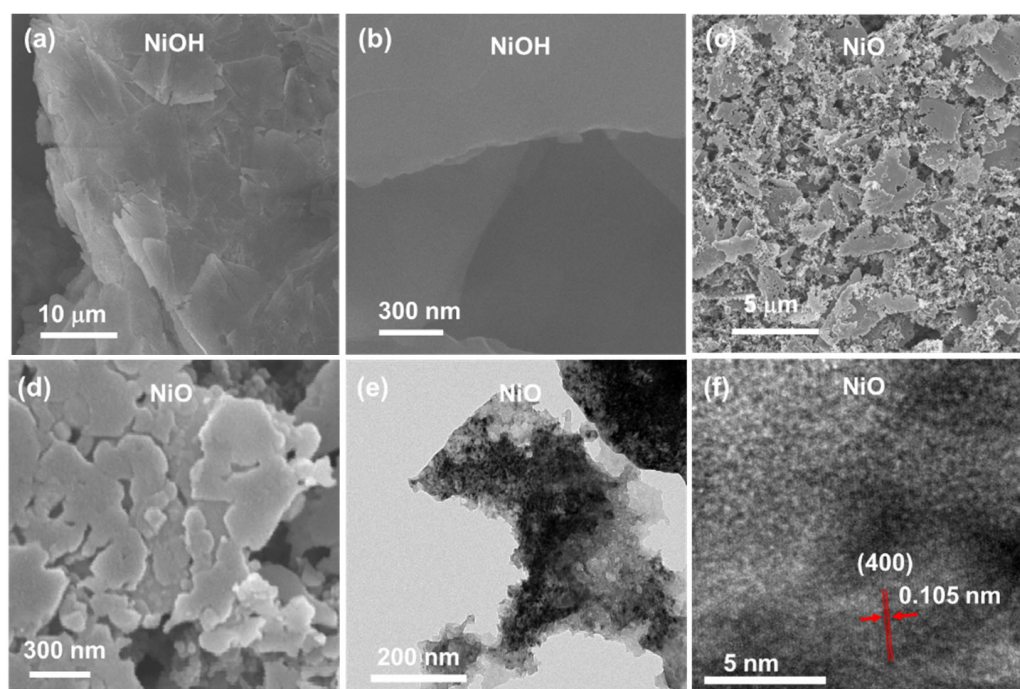

Figure 1. SEM images of Ni(OH)$_2$ NSs (**a**,**b**), NiO NSs (**c**,**d**), and TEM images of NiO NSs (**e**,**f**).

The detailed characteristics of the porous NiO NS structure can also be observed in the TEM image (Figure 1e), exhibiting layered NSs with several holes. In addition, the cubic phase of NiO is confirmed using a high-resolution TEM image, which showed a

spacing distance of 0.105 nm corresponding to the (004) plane in the NiO structure. Thus, the porous NiO NSs were well synthesized through quick calcination of $Ni(OH)_2$ at a high temperature of 600 °C. The adsorption—desorption isotherm plot of the BET measurements is shown in Figure S3a. The BET surface area is 9.4 m^2 g^{-1}, which is in good agreement with NiO obtained from $Ni(OH)_2$ annealed at a high temperature of 600–700 °C [56,57], and the pore volume of NiO is 0.022 cm^3 g^{-1}. In particular, the pore size of NiO heat-treated at 600 °C reached ~30 nm as in a previous report, but in this study, the pore size of NiO was found to be as low as 9.4 nm, which might be from the hydrothermal-assisted synthesis of $Ni(OH)_2$ [57]. The porosity of N1, N2, N3 and N4 anodes was also calculated based on the SEM images (Figure S3b–d), which are 13.6, 12.9, 12.1 and 12.4%, respectively. The difference in porosity was due to the random distribution of large NiO NSs.

As per our previous report, the porous NiO NSs, while being employed as anode materials for LIBs, showed significant capacity degradation and recovery under a current rate of 0.5 A g^{-1}. Ex situ measurements revealed that NiO is reconstructed into $LiNiO_2$ in a cycling process that promotes the insertion of lithium ions [28]. Its highly stable capacity was achieved owing to three main reasons (as discussed in the introduction): the conversion reaction of NiO, the increase in the surface area owing to the electrolyte derivation and the change in morphologies [28]. In this study, the restructuring of NiO to $LiNiO_2$ changed the morphologies and structure; therefore, the thickness of the anode can significantly affect the performance of the designed anode. It should be noted that the abnormal high capacity was observed at a high charge/discharge rate in many porous oxides-based anodes such as Fe_2O_3, Co_3O_4, SnO_2 [28,58–60]. Therefore, the criteria for the restructuring of NiO to $LiNiO_2$ might include high porosity with the affordable high current rate and the stability of the binder to maintain the structure. Figure 2 shows the cycling performance of N1, N2, N3 and N4 cells at 0.5 A g^{-1}. The healed state was recorded as the stable capacity of the cell following recovery from strong degradation after 100 cycles. During the initial 100 cycles, the capacity gradually degraded, owing to the development of a solid electrolyte interface (SEI) layer as well as active material loss or isolation during cycling [61]. Figure 2a demonstrates the restructuring process at 0.5 A g^{-1}, where a cycling test was performed until all the cells were stabilized. Following the required number of cycles to obtain the stable capacity state (reaching the restructuring state), the profile curves of N1, N2, N3, and N4 consist of a voltage plateau at 1.0–1.5 V in the discharge scan, and two voltage plateaus at 1.5 and 2.5 V in the charge scan (Figure 2b). These characteristic peaks are related to the electrochemical reactions of the restructured NiO NSs [62]. When the current rate increased, rapid degradation of the NiO anode occurred at the 100th cycle. Notably, the thinnest electrodes did not exhibit the fastest restructuring process (Figure 2c). However, the N1 electrode achieved the highest capacity of 1200 mAh g^{-1} after restructuring. The N2, N3, and N4 electrodes delivered capacities of 1000, 570, and 500 mAh g^{-1}, respectively. The theoretical capacity of NiO is ~720 mAh g^{-1}. Therefore, additional capacity was obtained for the thin electrodes. However, the electrode with thick layers deteriorated as a high current was applied, which could be because lithium ions were not effectively diffused into the material structure. Consequently, a few areas of the NiO NSs did not undergo lithium insertion/desertion, and were finally isolated, leading to the degradation of the overall performance of the cells.
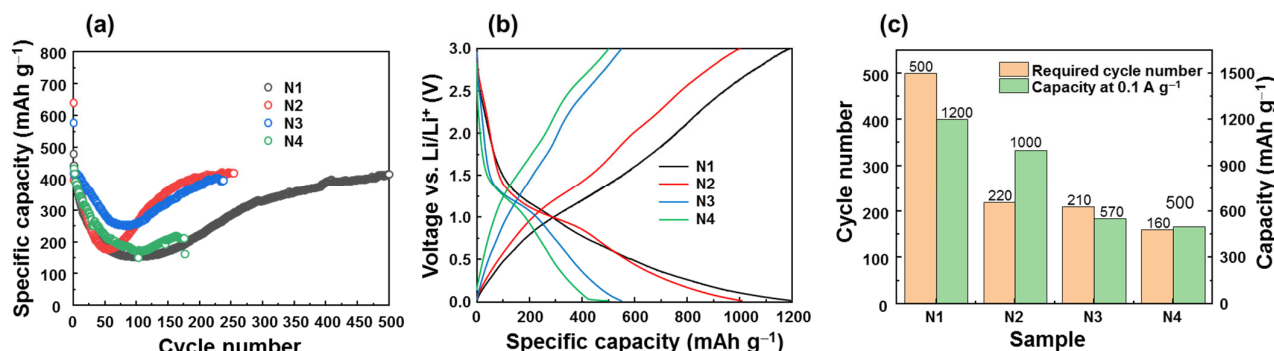
Figure 2. Cycling performance of restructuring process of NiO anodes at 0.5 A g^{-1} (**a**), voltage profiles of restructured anodes at 0.1 A g^{-1} (**b**), and plot of required number of cycles for restructuring and capacity at 0.1 A g^{-1} of NiO anodes (**c**).

Figure 3a shows the ex situ XRD patterns of N1, N2, N3, and N4 after the restructured states corresponding to 500, 220, 210, and 160 cycles, respectively. The restructured state of each electrode was compared with that of the bare NiO electrode. N1 and N2 anodes show a wide peak at ~18.5°, corresponding to the (003) plane. The enlarged XRD patterns of N1 and N2 in the range of 33–45° are shown in Figure S4. XRD peaks of LiNiO$_2$ appeared at 2θ = 36.2, 37.8 and 44.4° corresponding to (101), (006) and (104) planes, respectively. Following cycling, a part of the LiPF$_6$ electrolyte remained, forming a crystal structure on the surface of all electrodes [63]. In addition, weak peaks related to the LiNiO$_2$ phase were detected, confirming the restructuring of NiO into LiNiO$_2$ as previously reported [28]. Further, strong NiO peaks appear as the anode thickness increases, indicating an incomplete restructuring process. Meanwhile, the N3, N4 anodes only show weak peaks of LiNiO$_2$, indicating that the low amount of NiO was converted into LiNiO$_2$. Therefore, the restructuring process is only effective on the electrodes with relatively thin layers (N1 and N2). Figure 3b shows high-resolution digital optical images of the N1 and N2 electrodes in their initial states, as well as after the restructuring process. In their initial states, the N1 and N2 electrodes had thicknesses of 15.9, and 20.5 μm, respectively. After restructuring, the thicknesses of N1 and N2 were 20.3, and 25.0 μm, respectively, which corresponds to volume expansions of ~26.9%, and 25%, respectively. This indicates that during the restructuring process from NiO to LiNiO$_2$, the insertion of Li ions was accompanied by the expansion of NiO, forming a new structure together with the binder and conducting carbon. In contrast, the N3 and N4 electrodes had thicknesses of ~39.7, and 52.2 μm in their initial states. After restructuring, the thicknesses increased to 46.5, and 56.8 μm, corresponding to expansions of 17.1% and 8.8%, respectively. These results indicate that the smaller increase in the volume expansion could be attributed to the partial restructuring of NiO to LiNiO$_2$ for thick electrodes. Thus, the N1 samples with the thinnest layers exhibited a significant volume change, illustrating the superior restructuring of NiO to LiNiO$_2$. Based on these characteristics, the capacity of the N1 electrode increased to ~1200 mAh g^{-1} and the required cycle number for restructuring is 500 cycles. Meanwhile, the N2 anode required 220 cycles to reach the fully restructured state, and the capacity was still as high as 1000 mAh g^{-1}. The N3 and N4 electrodes exhibited rapid restructuring processes corresponding to 210 and 160 cycles, respectively. However, they exhibited low capacities of 570 and 500 mAh g^{-1}, respectively. This could be because the thick layers prevented the effective diffusion of Li ions; as a result, only part of the NiO was restructured into LiNiO$_2$. Therefore, the restructuring NiO of N3 and N4 anodes appeared to be faster than those of N1 and N2 anodes. Based on the previous report, the NiO anode could generally deliver a capacity of ~700 mAh g^{-1}. Therefore, this reduction in the cell capacity could be because the thick layers prevented the effective diffusion of Li ions; therefore, only part of the NiO was restructured into LiNiO$_2$. Finally, the non-restructured NiO was isolated from the restructured NiO, resulting in a significant decrease in capacity.
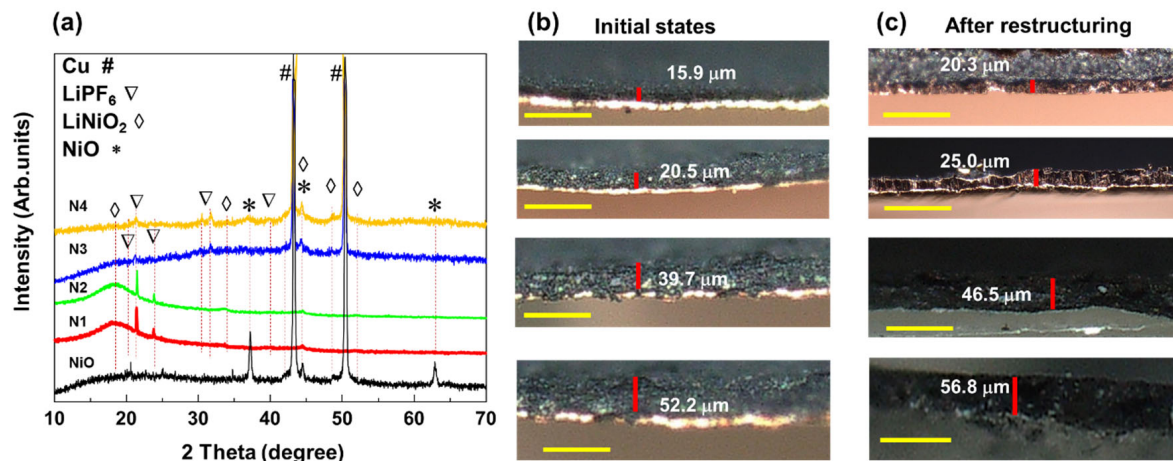
Figure 3. Ex situ XRD pattern of NiO anodes (**a**); digital optical images of cross sections of NiO anodes in their initial state (**b**) and after restructuring (**c**).

The diffusion coefficients of Li (D) in the restructured materials were measured using the GITT technique, as shown in Figure 4a,b. Furthermore, D was calculated based on the following equation [64]:

$$D = \frac{4}{\pi\tau} \left(\frac{m_B V_M}{M_B A}\right)^2 \left(\frac{\Delta E_S}{\Delta E_\tau}\right)^2, \tag{2}$$

where ΔE_S is the differential potential after the current pulse and steady state, ΔE_τ is the transient voltage changes due to the applied current for time t, m_B and M_B are the mass and molar mass of NiO active materials, V_M is the molar volume, and A is the effective area of the electrode. In this study, we assumed that all the active materials were restructured from NiO to LiNiO$_2$; therefore, the mass and volume were based on LiNiO$_2$ calculations. The D values of all samples are in the range of 10^{-14} to 10^{-10} cm^2 s^{-1}. During the discharging process in the N1 and N2 samples, D gradually decreases with the prevention of the initial states and reaches the lowest value at ~1.5 V, which is in good agreement with the rapidly decreasing potential in the voltage profile shown in Figure 2b. During the charging process, the D_{N1}, and D_{N2} values of N1, and N2 samples were approximately 10^{-10} cm^2 s^{-1} at 0 V, and decreased to ~10^{-12} with the increase in potential (~3.0 V). Two decreased peaks at 1.5 and 2.2 V were also observed as the desertion of Li occurred, corresponding to the voltage platform profiles in the charging process. D_{N3} exhibited the lowest values in the range of 2×10^{-13}–3×10^{-11} cm^2 s^{-1}. During discharging, D_{N3} continuously decreased after 1.5 V until the voltage reached 0 V. Similarly, during charging, D_{N3} continued to decrease as the potential increased. This indicates a harder insertion/desertion of Li in the N3 samples, which is related to the partial transformation of NiO to LiNiO$_2$, leading to the low performance in the electrochemical process. Figure 4c shows the high-rate performance of the N2 sample at 1.0 A g^{-1} for 500 cycles, delivering a capacity of 360–400 mAh g^{-1}. When the current decreased to 0.1 A g^{-1}, this anode still achieved a high capacity of 1000 mAh g^{-1}. Thus, the N2 anode rapidly achieved a restructuring state and retained its high-rate performance and high stability. The specific capacity of the N2 anode at 0.1 A g^{-1} is ~1000 mAh g^{-1}, which is 1.2 times less than that of the N1 anode (~1200 mAh g^{-1}). However, the active mass is 1.5 times higher than that of the N1 anode, meaning the N2 anode has a higher energy density. Therefore, it is more effective to use the N2 anode for commercialization to obtain viable lithium-ion cells.
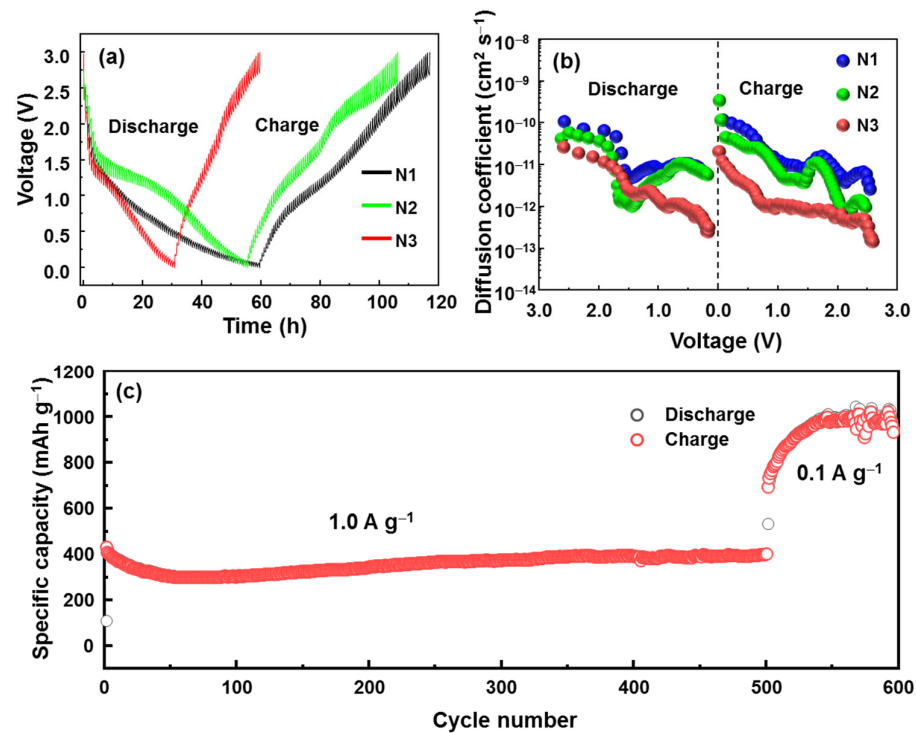
Figure 4. GITT measurement of restructured N1, N2, and N3 anodes (**a**), diffusion coefficient of restructured N1, N2, and N3 anodes (**b**), and cycling performance of N2 anodes for over 500 cycles at 1.0 A g^{-1} and 100 cycles at 0.l A g^{-1} (**c**).

The electrical properties of the electrodes with different thicknesses were further confirmed by impedance measurements, as shown in Figure 5a,b. The increase in the active loading mass from N1 to N4 increased the impedance values. The corresponding equivalent circuit contained series resistance (R$_S$), solid electrolyte interface layer resistance (R$_{SEI}$), charge transfer resistance (R$_{CT}$) with a Warburg diffusion element (W), and two constant-phase elements (CP1 and CP2), as shown in the inset of Figure 5b. The extracted R$_{CT}$ of samples N1, N2, N3, and N4 increased to 37.8, 59.8, 135.1, and 957.9 Ω, respectively. The significantly increased resistance of the N4 samples could be due to an affordable thick layer preventing the absorption of the electrolyte and diffusion of lithium ions. This could affect the restructuring process of the material, where the activated area was limited to a thickness exceeding 39.7 μm. Further confirmation of the lithium diffusion coefficient can be obtained using the following equations [65,66]:

$$D = \frac{R^2 T^2}{2n^4 F^4 \sigma_W^2 A^2 C^2} \tag{3}$$

where F is a Faraday constant, R is a gas constant; A is the effective area of the working electrode, and T is the working temperature (K); n is the number of electronic transports per material molecule, σ_W is the Warburg factor relative to the impedance of the cell, and C is the molar density of the charge carrier in the electrode.

The relation of impedance with the Warburg factor can be expressed using the following equation [67–69]:

$$Z' = R_T + \sigma_W \omega^{-1/2} \tag{4}$$

where R_T is the total resistance (R_T = R$_S$ + R$_{CT}$ + R$_{SEI}$), and ω is the measured angular frequency.

To evaluate and carry out a comparison with GITT, different setting voltages were applied to the EIS measurements in the range of 0.5–3.0 V, as shown in Figure 5b. The Warburg factor is proportional to the slope of the Z′($\omega^{-1/2}$) curve. The diffusion coefficient,

D, is proportional to σ^{-2}: Therefore, the increase in the slope in Figure 5c indicates a decrease in D as the voltage increases from 0.5 to 3.0V. These values are consistent with the GITT measurements. Therefore, the EIS and GITT measurements demonstrated an improvement in D_{Li} in the N1 and N2 samples, as well as a decrease in the thick anodes N3 and N4. Therefore, N2 showed an increased thickness compared to that of N1, but a comparable D_{Li} facilitates its use in practical applications.
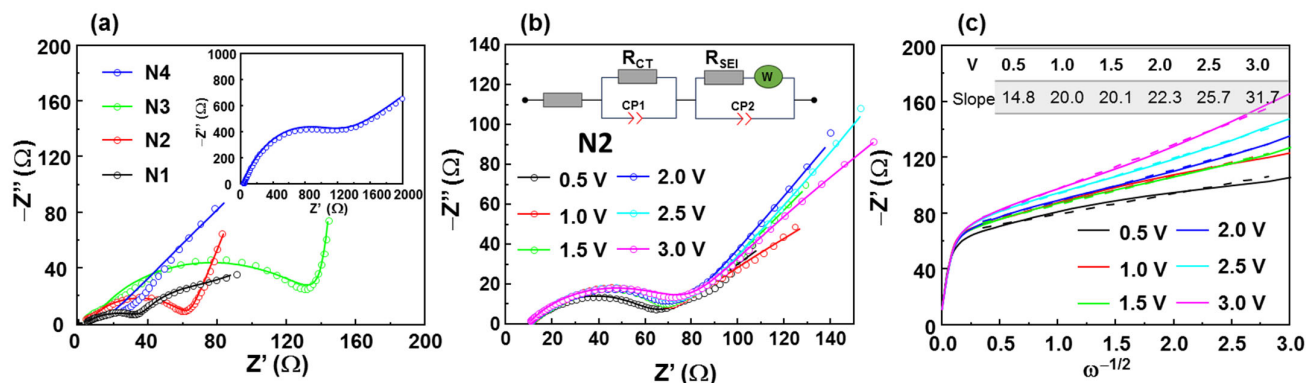

Figure 5. Nyquist plot of N1, N2, N3, N4 anodes (**a**), Nyquist plot of restructured N2 anode at different voltages (**b**), and Z' vs. $\omega^{-1/2}$ plots of N2 anodes at different voltages with dashed lines representing fitted curves(**c**).

Ex situ SEM images of the initial and post-restructuring states are shown in Figure 6. In the initial state, porous NiO was clearly observed. After cycling, the NiO structure transformed into the $LiNiO_2$/NiO structure, combining carbon and a PVDF network. Therefore, fringe patterns or layered structures were observed on the surfaces of samples N1 and N2. In contrast, the N3 anode exhibited an extremely rough surface with a non-uniform small and large particle mixture. From the results of the XRD pattern, a strong peak of NiO at $2\theta = 37.3°$ can be clearly observed in the case of N3 and N4 electrodes. It suggests that the existence of large particles on N3 and N4 anodes might have led to the partial transformation of NiO to $LiNiO_2$. These ex situ characteristics led to the conclusion that the capacity of thick-layer anodes was significantly decreased even though a stable state was formed. Therefore, restructuring NiO into $LiNiO_2$ is an effective strategy to achieve a highly stable anode material. As shown in Table 1, efficient phase transformation from NiO to $LiNiO_2$ requires careful control of the thickness of the NiO anode to approximately 20.5 μm. Although the effective thickness of NiO is currently low, this indicates that the mass loading can be increased if the conductivity of the anode material can be improved. Accordingly, a few additional improvement methods can be applied to circumvent this limitation, such as changing the additive materials or conductive polymers.

Table 1. Summarization of the thickness, volume expansion and electrochemical properties of N1, N2, N3, N4 anodes.

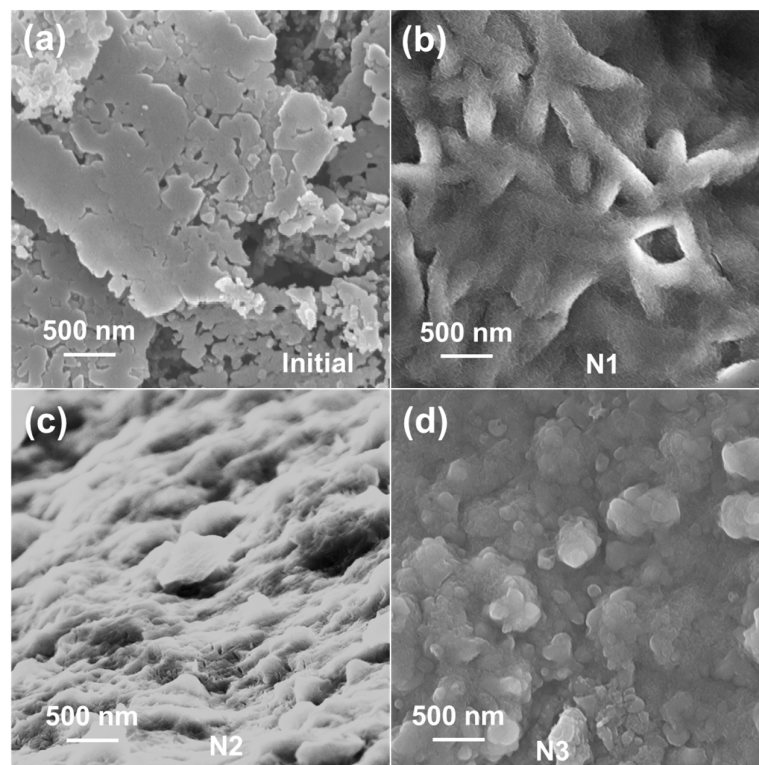| Sample Name	Thickness (μm)	Expanded Thickness (μm)	Restructuring Cycle Number	Capacity at 0.1 A g^{-1} (mAh g^{-1})
N1	15.9	20.3	500	1200
N2	20.5	25.0	220	1000
N3	39.7	46.5	210	570
N4	52.2	56.8	160	500

Figure 6. Ex situ SEM images of initial NiO anode (**a**), and restructured N1 (**b**), N2 (**c**), and N3 (**d**) anodes.

Research on NiO nanostructures for LIBs is summarized in Table 2. It is noted that the NiO nanostructure with a porous structure or with the support of a 3D porous structure can achieve high capacities of more than 800 mAh g^{-1}. The highest loading weight of the active material was about 1.5 mg cm^{-2}. Therefore, it is thought that restructured NiO anodes have comparable capacities to the currently used NiO anode materials. Although the thickness limitation is still an obstacle to practical application, it is thought that modifying the binder and size control of NiO can further improve the loading mass of the active material and improve the electrochemical performance of LIBs.

Table 2. Comparison of electrochemical performance of NiO nanostructures for LIBs.

Anode Materials	Morphology	Areal Weight of Active Material (mg cm^{-2})	Current Rate (A g^{-1})	Specific Capacity (mAh g^{-1})	References
NiO@CMK	NSs	-	0.1	1076	[42]
NiO/Ni foam	Nanobelt	1.3–1.5	~0.143	1035	[32]
NiO	Porous NSs	-	0.071	~800	[52]
NiO/Ni foam	Oxidation of Ni foam (NiO nanostructure)	-	~0.143	~750	[44,62]
NiO	Porous microtubules	1.42	0.2	~800	[29]
NiO	Nanoparticles	~1.0	0.1	~600	[70]
NiO	Nanoparticles	-	0.1	~730	[71]
NiO@C	Nanoparticles	1.5–2.5	0.1	~900	[43]
NiO/CNT	Nanoparticle assembled microsphere	-	0.1	~800	[72]
NiO	Porous NSs	1.5	0.1	1000	This work

4. Conclusions

In this work, NiO porous NSs were synthesized with a size range of 20 nm to several microns. The effect of NiO thickness on the restructuring of NiO to LiNiO$_2$ anodes for LIBs was investigated. A thickness limit of >39.7 μm was determined. Electrodes with thin NiO films (N1 and N2) with thicknesses of 15.9 and 20.5 μm (N1 and N2) were efficient at facilitating the transformation to LiNiO$_2$ with a capacity retention exceeding 1000 mAh g^{-1}. In addition, the diffusion coefficient of the thin anodes was in the range of 10^{-12}–10^{-10} cm^2 s^{-1}, which is much higher than that of the thick anodes (about 10 times). Ex situ XRD and SEM analyses also confirmed the non-uniform restructured surface of the thick anodes after cycling. This result indicates that the thickness of NiO should be controlled at approximately 20.5 μm to achieve an efficient LIB performance. To overcome this issue, additive materials, such as graphene or rGO, or the replacement of the PVDF binder can be used to achieve an efficient anode, which can enhance the conductivity of the thick film, facilitating the restructuring process of NiO to LiNiO$_2$.

Supplementary Materials: The following supporting information can be downloaded at: https://www.mdpi.com/article/10.3390/batteries10030080/s1. Figure S1. (a) SEM image of NiO NSs and (b) size distribution of NiO NSs. Figure S2. (a) XRD pattern of NiO NSs and (b) the Williamson–Hall plot from the XRD peaks. Figure S3. (a) Nitrogen adsorption–desorption isotherm plot of NiO NSs with the inset of pore volume distribution; (b–d) SEM images of N1, N2, N3, and N4 anodes, respectively. Figure S4. Enlarged XRD patterns in the range of 33–45 ° for N1 and N2 anodes.

Author Contributions: T.P.N.: Conceptualization, methodology, validation, visualization, writing, review, and editing. I.T.K.: Project administration, funding acquisition, review and editing. All authors have read and agreed to the published version of the manuscript.

Data Availability Statement: The data presented in this study are available upon request from the corresponding author to ensure integrity and prevent misunderstanding or misuse.

Conflicts of Interest: The authors declare no conflicts of interest.

References

1. Masuk, N.I.; Mostakim, K.; Kanka, S.D. Performance and emission characteristic analysis of a gasoline engine utilizing different types of alternative fuels: A comprehensive review. *Energy Fuels* **2021**, *35*, 4644–4669. [CrossRef]
2. Qazi, A.; Hussain, F.; Abd Rahim, N.; Hardaker, G.; Alghazzawi, D.; Shaban, K.; Haruna, K. Towards sustainable energy: A systematic review of renewable energy sources, technologies, and public opinions. *IEEE Access* **2019**, *7*, 63837–63851. [CrossRef]
3. Zantye, M.S.; Gandhi, A.; Wang, Y.; Vudata, S.P.; Bhattacharyya, D.; Hasan, M.M.F. Optimal design and integration of decentralized electrochemical energy storage with renewables and fossil plants. *Energy Environ. Mater.* **2022**, *15*, 4119–4136. [CrossRef]
4. Rostirolla, G.; Grange, L.; Minh-Thuyen, T.; Stolf, P.; Pierson, J.M.; Da Costa, G.; Baudic, G.; Haddad, M.; Kassab, A.; Nicod, J.M.; et al. A survey of challenges and solutions for the integration of renewable energy in datacenters. *Renew. Sustain. Energy Rev.* **2022**, *155*, 111787. [CrossRef]
5. Koohi-Fayegh, S.; Rosen, M.A. A review of energy storage types, applications and recent developments. *J. Energy Storage* **2020**, *27*, 101047. [CrossRef]
6. Nitta, N.; Wu, F.X.; Lee, J.T.; Yushin, G. Li-ion battery materials: Present and future. *Mater. Today* **2015**, *18*, 252–264. [CrossRef]
7. Masias, A.; Marcicki, J.; Paxton, W.A. Opportunities and challenges of lithium ion batteries in automotive applications. *ACS Energy Lett.* **2021**, *6*, 621–630. [CrossRef]
8. Zhao, L.; Zhang, T.; Li, W.; Li, T.; Zhang, L.; Zhang, X.; Wang, Z. Engineering of Sodium-Ion Batteries: Opportunities and Challenges. *Engineering* **2023**, *24*, 172–183. [CrossRef]
9. Goodenough, J.B.; Park, K.S. The Li-ion rechargeable battery: A perspective. *J. Am. Chem. Soc.* **2013**, *135*, 1167–1176. [CrossRef] [PubMed]
10. Liu, J.; Bao, Z.; Cui, Y.; Dufek, E.J.; Goodenough, J.B.; Khalifah, P.; Li, Q.; Liaw, B.Y.; Liu, P.; Manthiram, A.; et al. Pathways for practical high-energy long-cycling lithium metal batteries. *Nat. Energy* **2019**, *4*, 180–186. [CrossRef]

11. Hao, Y.; Shao, J.; Yuan, Y.; Li, X.; Xiao, W.; Sari, H.M.K.; Liu, T.; Lu, J. Design of phosphide anodes harvesting superior sodium storage: Progress, challenges, and perspectives. *Adv. Funct. Mater.* **2023**, *33*, 2212692. [CrossRef]

12. Kim, T.; Song, W.T.; Son, D.Y.; Ono, L.K.; Qi, Y.B. Lithium-ion batteries: Outlook on present, future, and hybridized technologies. *J. Mater. Chem. A* **2019**, *7*, 2942–2964. [CrossRef]

13. Evarts, E.C. Lithium batteries: To the limits of lithium. *Nature* **2015**, *526*, S93–S95. [CrossRef]

14. Goodenough, J.B.; Kim, Y. Challenges for rechargeable Li batteries. *Chem. Mater.* **2010**, *22*, 587–603. [CrossRef]

15. Arshad, F.; Li, L.; Amin, K.; Fan, E.; Manurkar, N.; Ahmad, A.; Yang, J.; Wu, F.; Chen, R. A comprehensive review of the advancement in recycling the anode and electrolyte from spent lithium ion batteries. *ACS Sustain. Chem. Eng.* **2020**, *8*, 13527–13554. [CrossRef]

16. Landi, B.J.; Ganter, M.J.; Cress, C.D.; DiLeo, R.A.; Raffaelle, R.P. Carbon nanotubes for lithium ion batteries. *Energy Environ. Mater.* **2009**, *2*, 638–654. [CrossRef]

17. Haregewoin, A.M.; Wotango, A.S.; Hwang, B.J. Electrolyte additives for lithium ion battery electrodes: Progress and perspectives. *Energy Environ. Mater.* **2016**, *9*, 1955–1988. [CrossRef]

18. Qian, H.; Li, X.; Chen, Q.; Liu, W.; Zhao, Z.; Ma, Z.; Cao, Y.; Wang, J.; Li, W.; Xu, K.; et al. $LiZn/Li_2O$ induced chemical confinement enabling dendrite-free Li-metal anode. *Adv. Funct. Mater.* **2023**, 2310143. [CrossRef]

19. Tang, Z.; Zhou, S.; Huang, Y.; Wang, H.; Zhang, R.; Wang, Q.; Sun, D.; Tang, Y.; Wang, H. Improving the initial coulombic efficiency of carbonaceous materials for Li/Na-ion batteries: Origins, solutions, and perspectives. *Electrochem. Energy Rev.* **2023**, *6*, 8. [CrossRef]

20. Karimzadeh, S.; Safaei, B.; Yuan, C.; Jen, T.-C. Emerging atomic layer deposition for the development of high-performance lithium-ion batteries. *Electrochem. Energy Rev.* **2023**, *6*, 24. [CrossRef]

21. Jia, H.; Li, X.; Song, J.; Zhang, X.; Luo, L.; He, Y.; Li, B.; Cai, Y.; Hu, S.; Xiao, X.; et al. Hierarchical porous silicon structures with extraordinary mechanical strength as high-performance lithium-ion battery anodes. *Nat. Commun.* **2020**, *11*, 1474. [CrossRef] [PubMed]

22. Tian, Y.; An, Y.; Feng, J. Flexible and freestanding silicon/MXene composite papers for high-performance lithium-ion batteries. *ACS Appl. Mater. Interfaces* **2019**, *11*, 10004–10011. [CrossRef]

23. Liu, J.; Xu, X.J.; Hu, R.Z.; Yang, L.C.; Zhu, M. Uniform hierarchical Fe_3O_4@polypyrrole nanocages for superior lithium ion battery anodes. *Adv. Energy Mater.* **2016**, *6*, 1600256. [CrossRef]

24. Luo, J.; Liu, J.; Zeng, Z.; Ng, C.F.; Ma, L.; Zhang, H.; Lin, J.; Shen, Z.; Fan, H.J. Three-dimensional graphene foam supported Fe_3O_4 lithium battery anodes with long cycle fife and high rate capability. *Nano Lett.* **2013**, *13*, 6136–6143. [CrossRef]

25. Li, Y.; Huang, Y.; Zheng, Y.; Huang, R.; Yao, J. Facile and efficient synthesis of α-Fe_2O_3 nanocrystals by glucose-assisted thermal decomposition method and its application in lithium ion batteries. *J. Power Sources* **2019**, *416*, 62–71. [CrossRef]

26. Jiang, T.; Bu, F.; Feng, X.; Shakir, I.; Hao, G.; Xu, Y. Porous Fe_2O_3 Nanoframeworks Encapsulated within Three-Dimensional Graphene as High-Performance Flexible Anode for Lithium-Ion Battery. *ACS Nano* **2017**, *11*, 5140–5147. [CrossRef]

27. Hassan, M.F.; Guo, Z.; Chen, Z.; Liu, H. α-Fe_2O_3 as an anode material with capacity rise and high rate capability for lithium-ion batteries. *Mater. Res. Bull.* **2011**, *46*, 858–864. [CrossRef]

28. Nguyen, T.P.; Giang, T.T.; Kim, I.T. Restructuring NiO to $LiNiO_2$: Ultrastable and reversible anodes for lithium-ion batteries. *Chem. Eng. J.* **2022**, *437*, 135292. [CrossRef]

29. Zheng, Y.; Li, Y.; Yao, J.; Huang, Y.; Xiao, S. Facile synthesis of porous tubular NiO with considerable pseudocapacitance as high capacity and long life anode for lithium-ion batteries. *Ceram. Int.* **2018**, *44*, 2568–2577. [CrossRef]

30. Jin, Y.; Zhu, B.; Lu, Z.D.; Liu, N.; Zhu, J. Challenges and recent progress in the development of Si anodes for lithium-ion battery. *Adv. Energy Mater.* **2017**, *7*, 1700715. [CrossRef]

31. Zhu, J.; Wang, T.; Fan, F.; Mei, L.; Lu, B. Atomic-scale control of silicon expansion space as ultrastable battery anodes. *ACS Nano* **2016**, *10*, 8243–8251. [CrossRef]

32. Hu, N.; Tang, Z.; Shen, P.K. Hierarchical NiO nanobelt film array as an anode for lithium-ion batteries with enhanced electrochemical performance. *Rsc Adv.* **2018**, *8*, 26589–26595. [CrossRef]

33. Ullah, K.; Shah, N.; Wadood, R.; Khan, B.M.; Oh, W.C. Recent trends in graphene based transition metal oxides as anode materials for rechargeable lithium-ion batteries. *Nano Trends* **2023**, *1*, 100004. [CrossRef]

34. Torres, R.M.; Manthiram, A. Delineating the effects of transition-metal-ion dissolution on silicon anodes in lithium-ion batteries. *Small* **2024**, e2309350. [CrossRef]

35. Lee, J.; Jeong, S.H.; Nam, J.S.; Sagong, M.; Ahn, J.; Lim, H.; Kim, I.-D. Toward thin and stable anodes for practical lithium metal batteries: A review, strategies, and perspectives. *EcoMat* **2023**, *5*, e12416. [CrossRef]

36. Shah, A.; Senapati, S.; Murthy, H.C.A.; Singh, L.R.; Mahato, M. Supercapacitor performance of NiO, NiO-MWCNT, and NiO–Fe-MWCNT composites. *ACS Omega* **2023**, *8*, 33380–33391. [CrossRef]

37. Li, C.; Choi, P.G.; Masuda, Y. Highly sensitive and selective gas sensors based on NiO/MnO_2@NiO nanosheets to detect allyl mercaptan gas released by humans under psychological stress. *Adv. Sci.* **2022**, *9*, 2202442. [CrossRef] [PubMed]

38. Itzhak, A.; He, X.; Kama, A.; Kumar, S.; Ejgenberg, M.; Kahn, A.; Cahen, D. NiN-passivated NiO hole-transport layer improves halide perovskite-based solar cell. *ACS Appl. Mater. Interfaces* **2022**, *14*, 47587–47594. [CrossRef] [PubMed]

39. Janus, W.; Ślęzak, T.; Ślęzak, M.; Szpytma, M.; Dróżdż, P.; Nayyef, H.; Mandziak, A.; Wilgocka-Ślęzak, D.; Zając, M.; Jugovac, M.; et al. Tunable magnetic anisotropy of antiferromagnetic NiO in (Fe)/NiO/MgO/Cr/MgO(001) epitaxial multilayers. *Sci. Rep.* **2023**, *13*, 4824. [CrossRef] [PubMed]

40. Gandhi, A.C.; Tummala, S.; Chiu, H.-H.; Ho, M.-K.; Li, T.-Y.; Chang, C.-K.; Cheng, C.-L.; Ho, Y.-P.; Wu, S.Y. Sm-doped NiO nanoparticles for magnetic memory at room temperature. *ACS Appl. Nano Mater.* **2021**, *4*, 10116–10127. [CrossRef]

41. Ata-ur, R.; Iftikhar, M.; Latif, S.; Jevtovic, V.; Ashraf, I.M.; El-Zahhar, A.A.; Abdu Musad Saleh, E.; Mustansar Abbas, S. Current advances and prospects in NiO-based lithium-ion battery anodes. *Sustain. Energy Technol. Assess.* **2022**, *53*, 102376. [CrossRef]

42. Fan, Z.Y.; Liang, J.; Yu, W.; Ding, S.J.; Cheng, S.D.; Yang, G.; Wang, Y.L.; Xi, Y.X.; Xi, K.; Kumar, R.V. Ultrathin NiO nanosheets anchored on a highly ordered nanostructured carbon as an enhanced anode material for lithium ion batteries. *Nano Energy* **2015**, *16*, 152–162. [CrossRef]

43. Wei, S.; Di Lecce, D.; Brescia, R.; Pugliese, G.; Shearing, P.R.; Hassoun, J. Electrochemical behavior of nanostructured NiO@C anode in a lithium-ion battery using $LiNi_{1/3}Co_{1/3}Mn_{1/3}O_2$ cathode. *J. Alloys Compd.* **2020**, *844*, 155365. [CrossRef]

44. Wang, X.H.; Sun, L.M.; Sun, X.L.; Li, X.W.; He, D.Y. Size-controllable porous NiO electrodes for high-performance lithium ion battery anodes. *Mater. Res. Bull.* **2017**, *96*, 533–537. [CrossRef]

45. Gan, H.H.; Zhang, Y.; Li, S.Q.; Yu, L.P.; Wang, J.R.; Xue, Z.G. Self-healing single-ion conducting polymer electrolyte formed via supramolecular networks for lithium metal natteries. *Acs Appl. Energy Mater.* **2021**, *4*, 482–491. [CrossRef]

46. Wang, C.; Wu, H.; Chen, Z.; McDowell, M.T.; Cui, Y.; Bao, Z. Self-healing chemistry enables the stable operation of silicon microparticle anodes for high-energy lithium-ion batteries. *Nat. Chem.* **2013**, *5*, 1042–1048. [CrossRef]

47. Jin, Y.; Li, S.; Kushima, A.; Zheng, X.; Sun, Y.; Xie, J.; Sun, J.; Xue, W.; Zhou, G.; Wu, J.; et al. Self-healing SEI enables full-cell cycling of a silicon-majority anode with a coulombic efficiency exceeding 99.9%. *Energy Environ. Mater.* **2017**, *10*, 580–592. [CrossRef]

48. Mezzomo, L.; Ferrara, C.; Brugnetti, G.; Callegari, D.; Quartarone, E.; Mustarelli, P.; Ruffo, R. Exploiting self-healing in lithium batteries: Strategies for next-generation energy storage devices. *Adv. Energy Mater.* **2020**, *10*, 2002815. [CrossRef]

49. Zhou, B.H.; Jo, Y.H.; Wang, R.; He, D.; Zhou, X.P.; Xie, X.L.; Xue, Z.G. Self-healing composite polymer electrolyte formed via supramolecular networks for high-performance lithium-ion batteries. *J. Mater. Chem. A* **2019**, *7*, 10354–10362. [CrossRef]

50. Nam, J.; Kim, E.; Rajeev, K.K.; Kim, Y.; Kim, T.H. A conductive self healing polymeric binder using hydrogen bonding for Si anodes in lithium ion batteries. *Sci. Rep.* **2020**, *10*, 14966. [CrossRef]

51. Chen, H.; Wu, Z.; Su, Z.; Chen, S.; Yan, C.; Al-Mamun, M.; Tang, Y.; Zhang, S. A mechanically robust self-healing binder for silicon anode in lithium ion batteries. *Nano Energy* **2021**, *81*, 105654. [CrossRef]

52. Li, Z.; Wei, L.; Liu, Y.; Su, Y.; Dong, X.; Zhang, Y. Facile synthesis of single-crystalline mesoporous NiO nanosheets as high-performance anode materials for Li-ion batteries. *J. Mater. Sci. Mater. Electron.* **2017**, *28*, 13853–13860. [CrossRef]

53. Kim, H.; Choi, W.; Yoon, J.; Um, J.H.; Lee, W.; Kim, J.; Cabana, J.; Yoon, W.S. Exploring anomalous charge storage in anode materials for next-generation Li rechargeable batteries. *Chem. Rev.* **2020**, *120*, 6934–6976. [CrossRef] [PubMed]

54. Heryanto; Hendri; Abdullah, B.; Tahir, D. Analysis of structural properties of X-ray diffraction for composite copper-activated carbon by modified Williamson-Hall and size-strain plotting methods. *J. Phys. Conf. Ser.* **2018**, *1080*, 012007. [CrossRef]

55. Kibasomba, P.M.; Dhlamini, S.; Maaza, M.; Liu, C.-P.; Rashad, M.M.; Rayan, D.A.; Mwakikunga, B.W. Strain and grain size of TiO_2 nanoparticles from TEM, Raman spectroscopy and XRD: The revisiting of the Williamson-Hall plot method. *Results Phys.* **2018**, *9*, 628–635. [CrossRef]

56. Wang, D.; Xu, R.; Wang, X.; Li, Y. NiO nanorings and their unexpected catalytic property for CO oxidation. *Nanotechnology* **2006**, *17*, 979. [CrossRef]

57. Wang, Z.; Shen, Q.; Xue, J.; Jia, H.; Xu, B.; Liu, X.; Li, Q. Annealing temperature effect on 3D hierarchically porous NiO/Ni for removal of trace hexavalent chromium. *Mater. Chem. Phys.* **2020**, *240*, 122140. [CrossRef]

58. Zhang, Z.; Li, W.; Ng, T.-W.; Kang, W.; Lee, C.-S.; Zhang, W. Iron(ii) molybdate ($FeMoO_4$) nanorods as a high-performance anode for lithium ion batteries: Structural and chemical evolution upon cycling. *J. Mater. Chem. A* **2015**, *3*, 20527–20534. [CrossRef]

59. Cao, B.; Liu, Z.; Xu, C.; Huang, J.; Fang, H.; Chen, Y. High-rate-induced capacity evolution of mesoporous $C@SnO_2@C$ hollow nanospheres for ultra-long cycle lithium-ion batteries. *J. Power Sources* **2019**, *414*, 233–241. [CrossRef]

60. Sun, H.; Xin, G.; Hu, T.; Yu, M.; Shao, D.; Sun, X.; Lian, J. High-rate lithiation-induced reactivation of mesoporous hollow spheres for long-lived lithium-ion batteries. *Nat. Commun.* **2014**, *5*, 4526. [CrossRef] [PubMed]

61. Carnovale, A.; Li, X. A modeling and experimental study of capacity fade for lithium-ion batteries. *Engergy AI* **2020**, *2*, 100032. [CrossRef]

62. Wang, X.; Li, X.; Sun, X.; Li, F.; Liu, Q.; Wang, Q.; He, D. Nanostructured NiO electrode for high rate Li-ion batteries. *J. Mater. Chem.* **2011**, *21*, 3571–3573. [CrossRef]

63. Nava, D.P.; Guzman, G.; Vazquez-Arenas, J.; Cardoso, J.; Gomez, B.; Gonzalez, I. An experimental and theoretical correlation to account for the effect of $LiPF_6$ concentration on the ionic conductivity of poly(poly (ethylene glycol) methacrylate). *Solid State Ion.* **2016**, *290*, 98–107. [CrossRef]

64. Lee, Y.-S.; Ryu, K.-S. Study of the lithium diffusion properties and high rate performance of $TiNb_6O_{17}$ as an anode in lithium secondary battery. *Sci. Rep.* **2017**, *7*, 16617. [CrossRef] [PubMed]

65. Rui, X.H.; Ding, N.; Liu, J.; Li, C.; Chen, C.H. Analysis of the chemical diffusion coefficient of lithium ions in $Li_3V_2(PO_4)_3$ cathode material. *Electrochim. Acta* **2010**, *55*, 2384–2390. [CrossRef]

66. So, S.; Ko, J.; Ahn, Y.N.; Kim, I.T.; Hur, J. Unraveling improved electrochemical kinetics of In_2Te_3-based anodes embedded in hybrid matrix for Li-ion batteries. *Chem. Eng. J.* **2022**, *429*, 132395. [CrossRef]

67. Piao, T.; Park, S.M.; Doh, C.H.; Moon, S.I. Intercalation of lithium ions into graphite electrodes studied by AC impedance measurements. *J. Electrochem. Soc.* **1999**, *146*, 2794–2798. [CrossRef]

68. Bisquert, J.; Garcia-Belmonte, G.; Bueno, P.; Longo, E.; Bulhões, L.O.S. Impedance of constant phase element (CPE)-blocked diffusion in film electrodes. *J. Electroanal. Chem.* **1998**, *452*, 229–234. [CrossRef]

69. Ye, B.; Xu, L.; Wu, W.; Ye, Y.; Yang, Z.; Ai, J.; Qiu, Y.; Gong, Z.; Zhou, Y.; Huang, Q.; et al. Encapsulation of 2D MoS_2 nanosheets into 1D carbon nanobelts as anodes with enhanced lithium/sodium storage properties. *J. Mater. Chem. C* **2022**, *10*, 3329–3342. [CrossRef]

70. Khalaji, A.D.; Jarosova, M.; Machek, P.; Chen, K.; Xue, D. Li-ion battery studies on nickel oxide nanoparticles prepared by facile route calcination. *Polyhedron* **2020**, *179*, 114360. [CrossRef]

71. Kumar Rai, A.; Tuan Anh, L.; Park, C.-J.; Kim, J. Electrochemical study of NiO nanoparticles electrode for application in rechargeable lithium-ion batteries. *Ceram. Int.* **2013**, *39*, 6611–6618. [CrossRef]

72. Xu, Y.; Hou, S.; Yang, G.; Lu, T.; Pan, L. NiO/CNTs derived from metal-organic frameworks as superior anode material for lithium-ion batteries. *J. Solid State Electrochem.* **2018**, *22*, 785–795. [CrossRef]